PAPER

Controllable fabrication of metallic photonic crystals for ultra-sensitive SERS and photodetectors†

Zihe Cai, Yang Yan, Lin Liu, Shengxuan Lin and Xiaobin Hu*

Metallic photonic crystals (MPCs), with extraordinary and controllable optical properties, are extremely desirable for optical sensors, solar energy conversion, ultrasensitive molecular detection and so on. Herein, a series of MPCs with inverse opal structure consisting of plasmonic metals (Ag and Cu) and transition metals (Ni and Co), respectively, are fabricated using a template-assisted electrochemical deposition method. In the UV-vis light region, plasmonic MPCs show tremendously strong multiple plasmon resonance made up of LSPR modes and Bragg modes. These extraordinary optical properties of MPCs are utilized to achieve ultra-sensitive detection (10^{-13} M, equivalent to ~0.094 molecules per μm^2 on average of the surface area) over a large area (≈ 1.0 cm^2) and a Raman signal enhancement factor of 1.9×10^{10}, suggesting that Ag MPCs are capable of single molecule detection. In addition, MPCs can act as efficient light absorbers and catalytically active sites in plasmon-induced direct photocurrent generation. A remarkable rise in photocurrent is observed as the light is switched on for Ag and Cu MPCs, which exhibits a high accordance with a linear model of optical power density.

1. Introduction

Metallic photonic crystals (MPCs), as artificial ordered nanostructures, have already attracted extensive attention due to their great potential in metamaterials,[1] extraordinary optical transmission (EOT),[2] optical sensors,[3] solar energy conversion[4] and molecular detection.[5] Highly ordered arrays of MPCs can be constitutive of various units such as nanoholes,[6] nanorods,[7] nanopyramids[8] and nanospheres.[9] A lot of attempts to achieve highly uniform MPCs of multiple structures have been made in recent years. For instance, laser etching,[10] lithography[11] and atomic layer deposition (ALD)[12] as top-down methods are widely used to fabricate 2D MPCs. These methods stand out because of their high uniformity and capacity to build various shapes, while the complex equipment required is non-negligible. In contrast, template-assisted self-assembly is a facile method to fabricate 3D MPCs.[13] The shape and period are determined by templates (*e.g.* colloidal crystals,[14] AAO,[15] or butterfly wings[16]) and the approaches to filling the voids around the template are multitudinous and attainable using nanoparticles,[17] original reducing[18] and electrodeposition.[19] Inverse opal,[20,21] also known as three-dimensional ordered macroporous (3DOM) arrays, is an interconnected hollow spheres nanostructure with face-centered cubic packing. The performance of inverse opal is

easily adjusted by varying the diameter and constituent materials. Nickel inverse opal shows more isotropic magnetic properties with enhanced coercivity which are attributed to domain wall pinning in the nickel network.[22] Moreover, MPCs exhibit characteristic optical properties when consisting of plasmonic metals (Au, Ag and Cu).[23–25] Pokrovsky and his coworkers[26] calculated the photonic band gap and reflectivity and transmission spectra of silver inverse opal, demonstrating that MPCs are capable of strong interactions with incident light through localized surface plasmon resonance (LSPR) modes and delocalized Bragg modes.[27] In simple terms, LSPR is made up of collective oscillations of free electrons in the metallic nanostructure driven by the electromagnetic field of incident light. LSPR and LSPR induced Landau damping have given rise to a new approach to the applications of MPCs for surface enhanced Raman scattering[28] and photocatalysis.[29,30] In addition, Bragg modes can couple intensively with LSPR modes leading to Fano resonance, which exhibits prominent performance for plasmonic sensing.[31]

Surface-Enhanced Raman Scattering (SERS) is one of the most powerful analytical techniques due to its capacity for single molecule detection[32] and providing high-resolution vibrational information[33] in comparison with fluorescence spectra. A promising SERS substrate should meet several requirements. Above all, elevated electromagnetic enhancement caused by LSPR is required to approach the detection limit for even single molecule detection where it is necessary to generate an enhancement factor (EF) of 10^8 to 10^{12}, assuming the same spectral sensitivity.[34] Next, the ability to be reproduced

State Key Laboratory of Metal Matrix Composites, Shanghai JiaoTong University, Shanghai 200240, People's Republic of China. E-mail: hxb@sjtu.edu.cn

and a facile fabrication method determine whether SERS substrates are suitable for practical application.[35] Generally, spatially isolated nanostructures do not provide a sufficient enhancement for single molecule detection.[36] Therefore, it is necessary to move towards the fabrication of strongly coupled nanostructures in order to achieve a giant field confinement in a highly localized nanoscale volume. In fact, MPCs with inverse opal structure may provide an additional enhancement due to tangential nanocavity arrays. When under illumination of incident light, elevated electromagnetic fields near the MPCs surfaces form, as caused by LSPR. In addition, metallic nano-cavities have a strong focusing effect of the electromagnetic field to the center of the nanocavities resulting in a co-focus effect.[37] The negative curvature confinement increases the plasmon energies because a greater electric field overlap is produced in the surrounding air, increasing the electromagnetic energy densities.

Despite the great coupling with light and remarkable performance that MPCs with inverse opal structure possess, systematic study on their fabrication and application is deficient. In addition, the effect of the MPC structure on performance is a significant issue to explore. To solve these problems, we propose a general strategy for the controllable fabrication of MPCs with inverse opal structure consisting of plasmonic metals (Ag and Cu) and transition metals (Ni and Co), respectively, which exhibit characteristic optical properties compared with dielectric photonic crystals. In the UV-vis light region, plasmonic MPCs efficiently harvested the incident light and showed multiple plasmon resonances made up of LSPR modes and Bragg modes. The photonic band gap is quite broad because of the enhanced optical penetration depth in the MPCs, compared with the skin depth of the pure metals. These optical properties could be easily controlled by changing the diameter of the MPCs, illustrating that it is beneficial for applications in SERS and photodetectors. For the Ag MPC sample of 200 nm diameter, ultra-sensitive detection (10^{-13} M, equivalent to $\sim$0.094 molecules per μm^2 on average of the surface area) over a large area ($\approx$1.0 cm^2) and an enhancement factor of 1.9×10^{10} were obtained, suggesting that Ag MPCs have great potential in achieving single molecule detection. In addition, MPCs could act as the light absorber and the catalytically active site in direct photocurrent generation. A remarkable rise in photocurrent was observed, when the light was switched on, in Ag and Cu MPCs which exhibited a significant rise in a linear model on optical power density, completely reversed compared with semiconductors.

2. Results and discussion

2.1. Fabrication of metallic photonic crystals

As depicted schematically in Scheme 1 the fabrication process of the MPCs consisted of three steps. Firstly, colloidal crystal templates were fabricated using self-assembling polystyrene (PS) monodisperse spheres with different diameters (200, 300, 370 and 450 nm) on FTO glass slides. PS was chosen for the templates for the following reasons: (a) it is convenient to synthesize monodisperse PS spheres; (b) the diameter of the PS
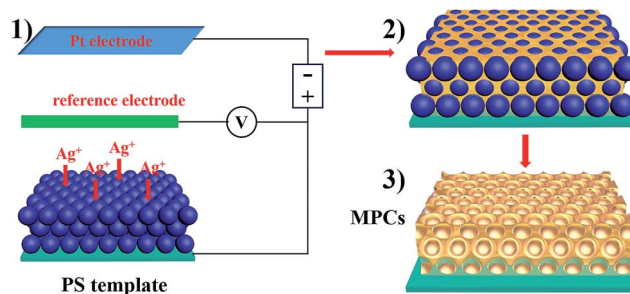
Scheme 1 Schematic of the fabrication procedures of metallic photonic crystals (MPCs) with inverse opal nanostructure. (1) Self-assembly of monodispersed PS spheres on FTO glass slides to form colloidal crystal templates; (2) the electrochemical deposition of metals (Ag, Cu, Ni and Co) into the voids around the colloidal crystal templates; (3) MPCs with interconnected nanocavity arrays after removing the templates in methylbenzene solution.

spheres is easy to adjust from nanometer to micrometer; (c) the electrostatic interaction between PS and FTO is strong enough to form high-quality films. After that, the FTO glass slides covered with colloidal crystal templates were used as working electrodes in 3-electrode systems. Before electrochemical deposition, the colloidal crystal templates were immersed in sodium dodecyl sulfate (SDS) solution (0.1 M) for 2 hours to enhance the hydrophilic property of the PS spheres, preventing the colloidal crystal templates from falling off due to stress. Subsequently, electrodeposition was carried out at room temperature for 5–10 min in order to fill the voids around the PS spheres with metal. When the electrodepositions were completed, the FTO glass slides with metal/PS composites were washed using deionized water to ensure no electrolyte remained and then immersed into methylbenzene solution for over 24 hours to remove the colloidal crystal templates. Ultimately, MPCs with face-centered cubic (FCC) nanopores were obtained.

Fig. S1a–d† show SEM images of the top layers of colloidal crystal templates composed of PS spheres. Each top layer was flat and the PS spheres were arranged with the (111) plane of the face-centered cubic (FCC) structure. The size of the PS spheres was adjusted from 200 nm to 450 nm easily by changing the dosage of styrene and methacrylic acid. A cross-sectional view of a colloidal crystal template is shown in Fig. S1e,† which illustrates that the number of layers of PS spheres was about 30 (8 μm of thickness). The reflection spectra demonstrate the photonic band gaps of the colloidal crystal templates with different diameters, resulting in different structure colors (Fig. S2†). Taking nickel photonic crystals for instance, the time current curve (Fig. 1a) shows the growth process of nickel on the FTO substrate covered with colloidal crystals. Nucleation occurred firstly on the surface of the FTO substrate (region I), where the current drops rapidly in a few seconds. After the nucleation step, nickel started to grow within the voids of the colloidal crystal template (region II). One can see a bowl structure before the nickel grew over the bottom layer (inset of Fig. 1a). Subsequently, nickel continued to fill the interspace among the PS spheres. Fig. 1b shows top-view SEM images of metallic photonic crystals on FTO substrates, composed of
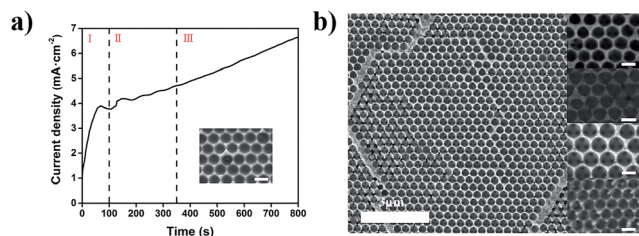
Fig. 1 (a) *I*–*t* curve of Ni electrodeposition into the voids of a colloidal crystal template on an FTO glass slide, with −0.95 V *vs.* Ag/AgCl electrode; (b) a large-area SEM image of the fabricated Ni MPC with a diameter of 300 nm, after 10 min of electrodeposition. The insets show magnified SEM images of Ag, Cu, Ni, and Co MPCs from top to bottom (scale bar of insets: 300 nm).

plasmonic metals (Ag, Cu) and transition metals (Ni, Co). After removing the colloidal crystal templates, interconnected nanoporous structures were obtained. The thickness of the Ag MPCs is about 2.5 μm after 5 min of deposition (Fig. S3†). The pore size of each MPC was determined from the diameter of the PS spheres. Meanwhile, the thickness of the MPCs was easily determined from the electro-deposition time.

2.2. Optical properties of metallic photonic crystals

The photographs and reflection spectra of the MPC films composed of different metals with different diameters (200, 300, 370 and 450 nm) show typical photonic band gaps like dielectric photonic crystals (Fig. 2a–g). The MPC films exhibited bright structure colors under illumination with white light. The photonic band gap was quite broad because of the enhanced optical penetration depth in the MPCs, compared with the skin
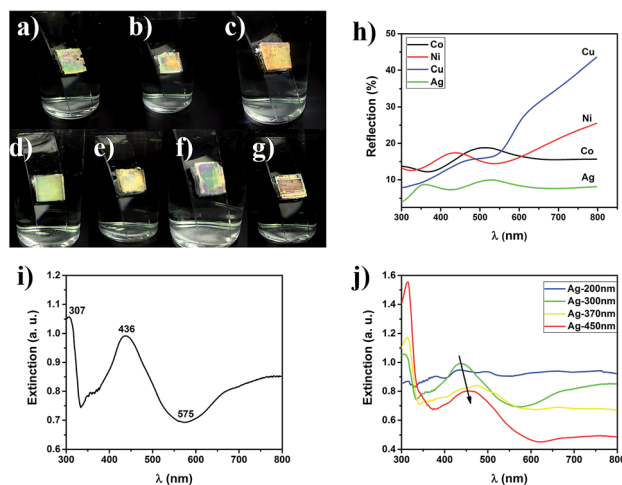
depth of the pure metals.[26] With the variation of the diameters from 200 nm to 450 nm, the structure colors of the Ag MPCs also changed from green to red which can be explained using Bragg's law.[38]

$$\lambda = \left(\frac{8}{3}\right)^{1/2} \times D \times \sqrt{(1-f)n_{air}^2 + f \times i \times \sigma/\omega - \sin^2\varphi} \qquad (1)$$

where, λ is the position of the reflectance peak. D is the center-to-center distance of the colloidal particles (or the diameter of the spheres), n and f are, respectively, the refractive index and the volume fraction of each component, σ is the metal conductivity, ω is the angular frequency, and φ is the angle between the incident beam and the sample normal. Therefore, structure color depends on both the diameter of the spheres and the refractive index of the materials. We measured reflection spectra of four kinds of MPC (Ag, Cu, Ni and Co) with the same diameter of 300 nm, in the UV-vis region. As shown in Fig. 2h, the reflection spectra of the MPCs exhibit broad reflection peaks which stand for the photonic band gaps. Due to the larger imaginary part of the reflective index, the photonic band gaps of the Ag and Cu MPCs were red shifted compared with the Ni and Co MPCs. Moreover, there is another reflectance peak on the left side of the band-gap in the spectra of the Ag or Cu MPC, which is due to localized surface plasmon resonance (LSPR). In order to further study the surface plasmon resonance (SPR) model, UV-vis extinction spectra of the Ag MPCs with diameters of 200, 300, 370 and 450 nm were measured (Fig. 2i and j). Multiple plasmon resonances were observed in the Ag MPCs in accordance with nanoprisms[39] and submicron particles.[40] Taking Ag-300 nm as an example, the trench at 570 nm in the spectrum is due to Bragg plasmons, which were generated because of the ordered structure of the MPC. The extinction peaks stand for Mie plasmons, which have energies that are highly dependent on the nanostructured geometry. The peak at 440 nm is the in-plane dipole plasmon resonance and the sharp peak at 320 nm is the out-plane quadrupole resonance because the position of the 320 nm peak did not change with the variation of the diameter as shown in Fig. 2j.[40] With regard to the Ag and Cu MPCs, the optical properties proved a combination of localized and delocalized plasmons which are termed as "Mie plasmons" and "Bragg plasmons", respectively.[41] Furthermore, with the diameter extending from 200 nm to 450 nm the major LSPR peak and Bragg peak were both red shifted, at the same time the extinction ratio dropped in the visible light region which meant weaker interaction between the incident light and the Ag MPCs *via* LSPR.

2.3. Ultra-sensitive SERS detection of R6G

To explore the application prospect of the strong interaction of MPCs with incident light, a series of Raman spectra were measured using an active fluorescent molecule, rhodamine 6G (R6G), as a probe and Ag MPCs (diameters of 200, 300, 370 and 450 nm) as SERS substrates in order to experimentally confirm the predicted large signal enhancement. All of the Raman spectra were collected from 1 cm² areas of the samples. As shown in Fig. 3a, the Raman spectra of R6G (concentration of

Fig. 2 (a–c) Photographs of the structure colors of Ni, Co and Cu MPC films on FTO glass slides immersed in ethyl alcohol solution, with the same diameter of 300 nm; (d–g) photographs of the structure colors of Ag MPC films on FTO glass slides with diameters of 200, 300, 370 and 450 nm, respectively; (h) experimental UV-vis reflection spectra of Ni, Cu, Ag and Cu MPCs; (i) experimental UV-vis extinction spectrum of a Ag MPC with a diameter of 300 nm; (j) experimental UV-vis extinction spectra of Ag MPCs with various diameters of 200, 300, 370 and 450 nm.
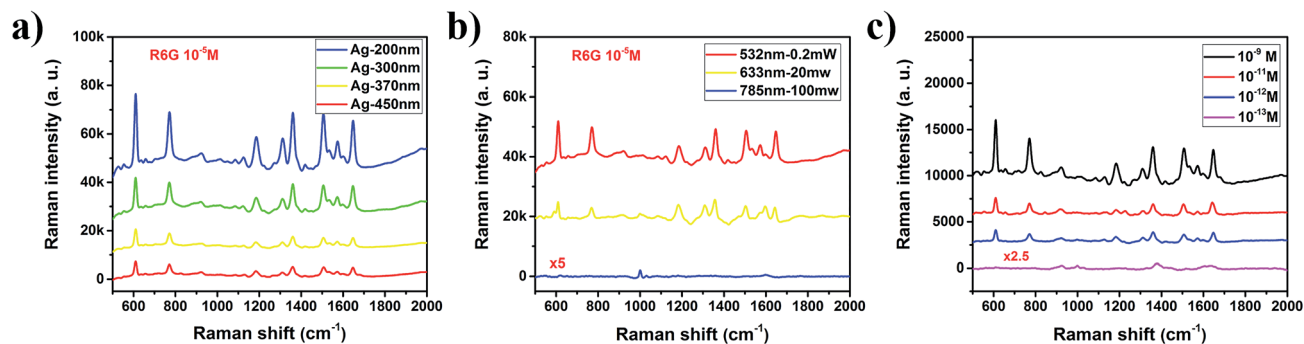
Fig. 3 (a) Measured Raman spectra of 10^{-5} M R6G on Ag MPCs with various diameters of 200, 300, 370 and 450 nm; under excitation of 532 nm wavelength and a 0.2 mW laser; (b) the measured Raman spectra of the Ag-300 nm MPC were measured under different incident light (532, 633 and 785 nm); (c) the measured Raman spectra of R6G on Ag-200 nm MPCs with 4 different concentrations (10^{-9} M, ~940 molecules per μm², 10^{-11} M, ~9.4 molecules per μm², 10^{-12} M, ~0.94 molecules per μm², and 10^{-13} M, ~0.094 molecules per μm²).

10^{-5} M) displayed eight prominent Raman peaks. The peaks at 1313 cm⁻¹, 1362 cm⁻¹, 1507 cm⁻¹ and 1648 cm⁻¹ were assigned to C–C stretching modes which had the largest enhancement factors of 7–10 with the diameter of the Ag MPCs varying from 450 nm to 200 nm, unambiguously demonstrating a significantly improved SERS sensitivity.[8] The peak at 613 cm⁻¹ was assigned to the C–C–C deformation in-plane vibration, with 775 cm⁻¹ and 1187 cm⁻¹ (the out-of-plane and in-plane vibrations of deformed C–H bonds) showing weaker enhancement factors of 4–5. These observations illustrate how the MPC structure affects SERS. Firstly, high-density hotspots form due to the strong LSPR of the ordered nanopores when Ag MPCs are under illumination of 532 nm wavelength incident light. In addition, the metallic nanocavities have a strong focusing effect of the electromagnetic field to the centers of the nanocavities resulting in a co-focus effect.[37,42] The negative curvature confinement increases the plasmon energies because a greater electric field overlap is produced in the surrounding air, increasing the electromagnetic energy densities. Moreover, the SERS enhancement factor was 4–10 times higher with the diameter varying from 200 nm to 450 nm, which was highly in accordance with the results of the extinction spectra. In order to illustrate the impact of the incident light, the Raman spectra of the Ag-300 nm MPC were measured using different incident light (as shown in Fig. 3b). One can see that the intensity of the Raman scattering under 633 nm incident light was much weaker than that under 532 nm incident light, even on increasing the luminous power from 0.2 mW to 20 mW. In addition, there was only one distinct peak at 997 cm⁻¹ which is potentially due to a charge transfer mechanism between the Ag MPCs and R6G molecules because the light at 785 nm wavelength is far away from the LSPR peak of Ag MPCs according to the extinction spectrum. The detection limit is one of the most important parameters for evaluating the overall performance of a SERS substrate. To explore the limit of detection of the MPCs, we measured Raman spectra with varying concentrations of R6G from 10^{-9} M to 10^{-13} M, using Ag-200 nm as an example. As shown in Fig. 3c, even with a concentration down to 10^{-13} M (equivalent to ~0.094 molecules per μm² on average of the surface area), the Raman peaks at 1362 cm⁻¹ and 1648 cm⁻¹ of

R6G SERS were still visible as well as the other peaks which appeared again when the concentration rose to 10^{-12} M (equivalent to ~0.94 molecules per μm² on average of the surface area). Furthermore, the enhancement factor (EF) is another significant parameter of SERS substrates. In order to estimate the EF of Ag MPCs, we determined enhancement factor as a specific value from the measured SERS intensities and non-enhanced Raman scattering intensities under the same conditions, as in eqn (2)[43]

$$EF = (N_{NE} \times I_{SERS})/(N_{SERS} \times I_{NE}) \qquad (2)$$

where I_{SERS} and I_{NE} correspond to the SERS intensities and non-enhanced Raman scattering intensities, respectively, and N_{NE} and N_{SERS} are the number of molecules probed in a bulk sample and that were adsorbed on the Ag MPCs. Then, the EFs of the Ag MPC substrates were measured by diluting R6G solutions of 10^{-12} M and 10^{-13} M with 532 nm laser excitation. As a reference, a 50 μL droplet of 0.01 M R6G solution was deposited on a normal Ag film substrate for Raman scattering measurement (Fig. S4†). The probe molecules (R6G) were assumed to disperse uniformly on the substrates. Ultimately, the EFs of the Raman peaks are listed in Table 1 with an outstanding average value of 7.6×10^9. To be specific, the peak at 1648 cm⁻¹ had the largest EF of 1.9×10^{10} while the peak at 1607 cm⁻¹ had the weakest EF of 2.3×10^9 in contrast. The EF in this work is one or two orders of magnitude higher than that of various noble metal nanostructures in the literature (Table S1†).

Table 1 EFs of Ag-200 nm MPCs at different Raman peaks

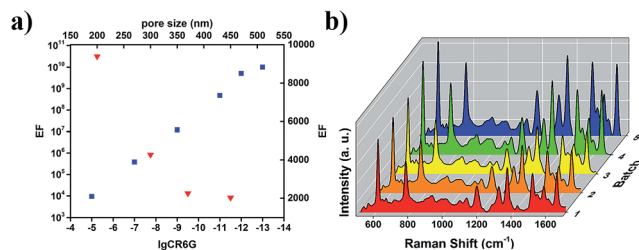| Peak position (cm⁻¹)	EF
613	4.8×10^9
771	5.8×10^9
1187	3.8×10^9
1362	1.0×10^{10}
1607	2.3×10^9
1648	1.9×10^{10}

Fig. 4 (a) Scatter diagram of the EF at 1648 cm^{-1} as a function of concentrations ranging from 10^{-5} M to 10^{-13} M and the EF of Ag MPCs with different pore sizes; (b) Raman spectra of 10^{-7} M R6G collected from five Ag-200 nm MPC substrates of different batches.

Fig. 4a reveals the impact of concentration and pore size. Firstly, the EF exhibited a dramatic increase as the R6G molecule concentration decreased which was due to the insufficient adsorption of R6G molecules onto the Ag MPC substrate at high concentration. Secondly, the calculated logarithmic value of the EF maintained a linear relation to the logarithmic value of the R6G molecule concentration (C_{R6G}), indicating that the EF can be estimated at a given analyte concentration and that Ag MPCs are highly attractive substrates for quantitative purposes. What's more, the EF exhibited a dramatic decrease with the pore size increasing from 200 to 450 nm. From the above, both the detection limit (10^{-13}M, ~0.094 molecules per µm^2) and EF (2.3×10^9–1.9×10^{10}) suggest that Ag MPCs have great potential in achieving single molecule detection. In order to further prove our speculation, three different positions on one Ag-200 nm sample were chosen randomly for SERS measurement, with an R6G concentration of 10^{-13} M. As shown in Fig. S5,† only selective peaks (925 cm^{-1}, 1000 cm^{-1}, 1380 cm^{-1} and 1633 cm^{-1}) with narrower linewidths are visible in position 2 and 3. Moreover, the positions, relative intensities and linewidths of these peaks exhibited clear variation because of the various orientations on the different surfaces due to the numerous possible coordinating sites, which is a typical characteristic of single molecule detection.[44] To evaluate the reproducibility of the Ag MPC substrate, we measured Raman spectra of five different batches, as shown in Fig. 4b, and the Raman signal was stable and the relative standard deviation (RSD) of the intensity was less than 20% for the 613 cm^{-1} peak, confirming a good reproducibility for the Ag MPCs substrate.

2.4. Photocurrent responses of the metallic photonic crystals

LSPR nanostructures like MPCs have widespread applications in photocatalysis,[45] solar energy conversion[46] and photodetectors.[47] On one hand, the excitation of LSPR is used to transfer photon energy to nearby semiconductors,[48] molecular photocatalysts, and other metals to drive chemistry remotely. On the other hand, LSPR nanostructures can act as the light absorber and the catalytically active site.[49] To assess the performance of the MPCs in direct photocurrent generation, MPC samples with diameters of 200, 300, 370 and 450 nm composed of different metals (Ag, Cu and Ni) were characterized under the

illumination of white light (300 mW cm^{-2}). The measurement was carried out in a three-electrode system in which the MPC films acted as the working electrode, a platinum plate acted as a counter electrode, Ag/AgCl was used as a reference electrode and KCl (0.2 M) solution was the electrolyte. As shown in Fig. 5a, a remarkable rise in the photocurrent was observed in the Ag and Cu MPCs when the light was switched on, while there was no photocurrent observed in the Ni MPC, predictably due to its sluggishness in visible light. What's more, Ag-200 nm MPCs had the greatest rise of 10-fold in the photocurrent while the Ag-450 nm MPCs had only 3-fold rise in comparison under the same conditions. Obviously, the efficiency of light harvesting of the MPCs determines the photocurrent generation. As a photodetector, response time (τ_R) and recovery time (τ_D) are two key characteristic parameters, where τ_R represents the time needed to approach 63% ($\approx 1 - e^{-1}$) of the value of the maximum photocurrent from the dark current, and τ_D is defined as the time needed for recovery to 37% ($\approx e^{-1}$) of the maximum photocurrent. The calculated τ_R and τ_D were 1.8 s and 1.0 s for the Ag-200 nm MPCs photodetector, and 1.2 s and 1.0 s for the Ag-450 nm MPCs photodetector, respectively. From the above, the diameter of the Ag MPCs had a weak effect on τ_R and τ_D in
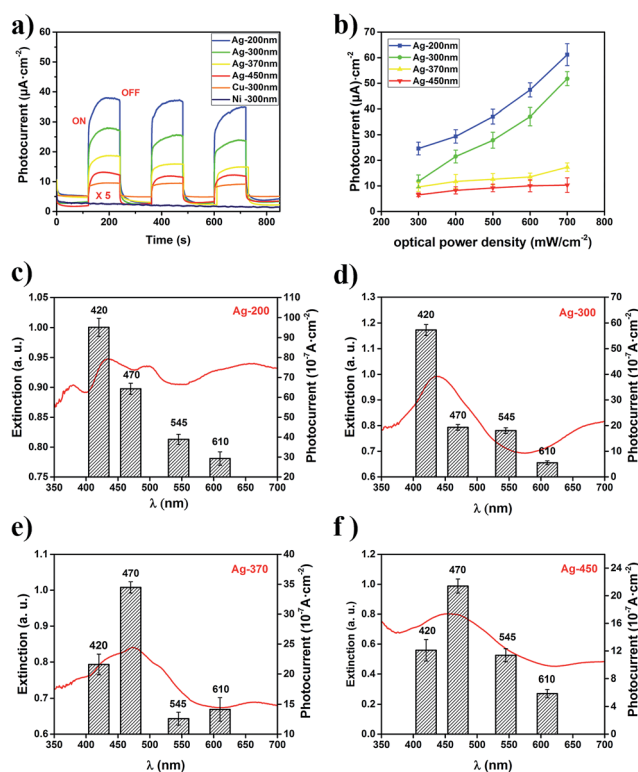

Fig. 5 (a) Amperometric I–t curves collected for Ag MPCs with various diameters of 200, 300, 370 and 450 nm, a Cu-300 nm MPC and a Ni-300 MPC under the illumination of white light (300 mW cm^{-2}); (b) photocurrent plots of Ag MPCs with various diameters of 200, 300, 370 and 450 nm under illumination of different optical power densities from 300 to 700 mW cm^{-2}; (c–f) bar graphs of the photocurrents of the above-mentioned Ag MPCs under the illumination of monochromatic light of different wavelengths (420, 470, 545 and 610 nm): (c) 200 nm; (d) 300 nm; (e) 370 nm; (f) 450 nm.

spite of the strong effect of photocurrent generation. When we adjusted the optical power density from 300 mW cm^{-2} to 700 mW cm^{-2}, the photocurrent showed a significant rise in a linear model (Fig. 5b). However, the photocurrent of the Ag-200 nm MPCs and Ag-300 nm MPCs had a greater rise rate than the other two MPCs. To explain this phenomenon, we consider the effect of light illumination in two parts. (a) The generation of hot electrons due to LSPR; (b) the enhancement of the temperature field due to the illumination. It needs to be stated in advance that the rate and quantum efficiency of photocatalytic reactions of metallic nanostructures increase with operating temperature. For Ag-200 nm and Ag-300 nm MPCs, LSPR plays a more significant role in photocatalytic reactions due to stronger responses to photon reactions resulting in greater rises in the rates of the photocurrents.

For the sake of proving that the photocurrent generation results from LSPR of the MPCs stimulated by incident light, the photocurrents of the Ag MPCs were measured under monochromatic light of different wavelengths (420, 470, 545, and 610 nm) with the same optical power density (100 mW cm^{-2}). As shown in Fig. 5c–f, the variation trend of the photocurrent of Ag MPCs (with diameters of 200, 300, 370 and 450 nm) was in high accordance with the LSPR in the extinction spectra. For instance, for Ag-300 nm MPCs in Fig. 5d, the highest photocurrent appears at the 420 nm wavelength position in contrast with the 470 nm wavelength of Ag-370 nm (Fig. 5e) because the LSPR peak varies from 434 nm to 470 nm. Detailed mechanisms of photocurrent generation of plasmonic metallic nanostructures have been intensively studied and summarized by Christopher and coworkers.[30] Plasmons decayed through Landau damping, where photon energy is converted to single electron/hole pair excitations, occurring ca. 10 fs after the initial plasmon excitation. Subsequently, energetic electrons were directly injected into adsorbate states at the instant of plasmon dephasing, occurring on the scale of ca. 5 fs.

3.   Conclusions

In summary, we have fabricated a series of MPCs with highly uniform inverse opal structure consisting of plasmonic metals (Ag and Cu) and transition metals (Ni and Co), respectively, by a self-assembly and electrochemical deposition method. The MPCs exhibited characteristic and controllable optical properties illustrating that MPCs can act as great light absorbers due to LSPR for high electromagnetic field enhancement or dense plasmonic hot spots and energetic electron generation. Moreover, MPCs have been applied for ultrasensitive molecule detection as SERS substrates. A high detection limit (10^{-13}M, equivalent to ~0.094 molecules per μm^2 on average of the surface area) over a large area (≈ 1.0 cm^2) was achieved by changing the diameter of the nanocavities, and great reproducibility was proven. Plasmons decayed through Landau damping, where photon energy is converted to single electron/hole pair excitations, then energetic electrons were directly injected into adsorbate states at the instant of plasmon dephasing. In light of the above facts, our work opens up great opportunities to MPCs for potential applications in ultrasensitive SERS and photodetectors.

4.   Experimental section

4.1.   Fabrication of the metallic photonic crystals

Monodispersed PS spheres were synthesized using emulsion polymerization, in which styrene was the monomer, potassium persulfate was an initiator and methacrylic acid was a surfactant. Self-assembly of the PS spheres onto FTO glass slides (50 × 10 mm^2) was carried out through vertical deposition methods in deionized water under 50 °C and 55% RH to form colloidal PS crystals. Before electrochemical deposition, the colloidal crystal templates were immersed into sodium dodecyl sulfate (SDS) solution (0.1 M) for 2 hours to enhance the hydrophilic property of the PS spheres, preventing the colloidal crystal templates from falling off because of stress. The electrodeposition of Ag was performed via a galvanostatic method at a current density of 2.5 mA cm^{-2} for 5 min in an Ag plating solution containing 0.1 M AgNO$_3$, 0.1 M EDTA, 0.15 M boric acid, 0.2 M potassium nitrate and 80 g L^{-1} ammonium hydroxide (pH $\approx$ 9.0) at approximately 25 °C. The details of the electrodeposition of the other metals are provide in the ESI.† After the electrodeposition, the FTO glass slides with metal/PS composites were washed with deionized water, to ensure that no electrolyte remained, and then immersed into methylbenzene solution for over 24 hours to remove the colloidal crystal templates.

4.2.   Characterization

The morphologies of the surfaces of the MPC samples were investigated using a super resolution field emission scanning electron microscope (JEOL JSM-7800F Prime). Reflection and extinction spectra of the colloidal crystals and MPCs were collected using a UV-vis-NIR spectrophotometer (Lambda 950) setup for a range of 300–800 nm. To evaluate the SERS efficiency of the Ag MPCs, R6G solution (50 μL) in ethyl alcohol (10^{-5}–10^{-13} M, respectively) was dropped in five 10 μL portions onto the substrates. After drying under ambient conditions, micro-Raman spectra were carried out using a dispersive Raman microscope (Senterra R200-L) under ambient conditions. The laser excitation wavelength was 532 nm from a He–Ne laser. The diameter of the laser spot was 2 μm. The power of the laser and accumulation time were kept around 0.2 mW and 2 s for a single spectrum. The photocurrent was measured using a time current curve (I–t) at 25 °C using an electrochemical workstation (CHI660E), in which the open circuit potential was set as the initial potential. The measurement was carried out in a three-electrode system in which an MPC film was the working electrode, a platinum plate was the counter electrode, Ag/AgCl was a reference electrode and KCl (0.2 M) solution was the electrolyte. A shutter was used to switch on/off the light with an adjustable optical power density by current value derived from a xenon lamp as the light source.

Conflicts of interest

There are no conflicts to declare.

Acknowledgements

Notes and references

1 O. Hess, J. B. Pendry, S. A. Maier, R. F. Oulton, J. M. Hamm and K. L. Tsakmakidis, *Nat. Mater.*, 2012, **11**, 573–584.
2 Y. Fang, V. W. Chen, Y. Cai, J. D. Berrigan, S. R. Marder, J. W. Perry and K. H. Sandhage, *Adv. Funct. Mater.*, 2012, **22**, 2550–2559.
3 X. Zhang, S. Feng, J. Zhang, T. Zhai, H. Liu and Z. Pang, *Sensors*, 2012, **12**, 12082–12097.
4 Z. Zhan, F. Grote, Z. Wang, R. Xu and Y. Lei, *Adv. Energy Mater.*, 2015, **5**, 1501654.
5 H. Im, K. C. Bantz, S. H. Lee, T. W. Johnson, C. L. Haynes and S. H. Oh, *Adv. Mater.*, 2013, **25**, 2678–2685.
6 T. Sannomiya, O. Scholder, K. Jefimovs, C. Hafner and A. B. Dahlin, *Small*, 2011, **7**, 1653–1663.
7 J. Li, S. K. Cushing, P. Zheng, F. Meng, D. Chu and N. Wu, *Nat. Commun.*, 2013, **4**, 2651.
8 P. Wang, O. Liang, W. Zhang, T. Schroeder and Y. H. Xie, *Adv. Mater.*, 2013, **25**, 4918–4924.
9 E. Armstrong and C. O'Dwyer, *J. Mater. Chem. C*, 2015, **3**, 6109–6143.
10 W. Zhou and T. W. Odom, *Nat. Nanotechnol.*, 2011, **6**, 423–427.
11 H. C. Jeon, C.-J. Heo, S. Y. Lee and S.-M. Yang, *Adv. Funct. Mater.*, 2012, **22**, 4268–4274.
12 V. Rinnerbauer, A. Lenert, D. M. Bierman, Y. X. Yeng, W. R. Chan, R. D. Geil, J. J. Senkevich, J. D. Joannopoulos, E. N. Wang, M. Soljačić and I. Celanovic, *Adv. Energy Mater.*, 2014, **4**, 1400334.
13 M. M. Hossain and M. Gu, *Laser Photonics Rev.*, 2014, **8**, 233–249.
14 O. H. Kim, Y. H. Cho, S. H. Kang, H. Y. Park, M. Kim, J. W. Lim, D. Y. Chung, M. J. Lee, H. Choe and Y. E. Sung, *Nat. Commun.*, 2013, **4**, 2473.
15 X. Zhang, Y. Zheng, X. Liu, W. Lu, J. Dai, D. Y. Lei and D. R. MacFarlane, *Adv. Mater.*, 2015, **27**, 1090–1096.
16 Y. Tan, J. Gu, X. Zang, W. Xu, K. Shi, L. Xu and D. Zhang, *Angew. Chem., Int. Ed.*, 2011, **50**, 8307–8311.
17 L. Zhang, C. Y. Lin, V. K. Valev, E. Reisner, U. Steiner and J. J. Baumberg, *Small*, 2014, **10**, 3970–3978.
18 L. Lu and A. Eychmuller, *Acc. Chem. Res.*, 2008, **41**, 244.
19 T. Sun, C. Zhang, J. Chen, Y. Yan, A. A. Zakhidov, R. H. Baughman and L. Xu, *J. Mater. Chem. A*, 2015, **3**, 11367–11375.
20 H. Zhang, X. Yu and P. V. Braun, *Nat. Nanotechnol.*, 2011, **6**, 277–281.
21 P. M. Wilson, G. N. Mbah, T. G. Smith, D. Schmidt, R. Y. Lai, T. Hofmann and A. Sinitskii, *J. Mater. Chem. C*, 2014, **2**, 1879.
22 P. N. Bartlett, M. A. Ghanem, I. S. El Hallag, P. de Groot and A. Zhukov, *J. Mater. Chem.*, 2003, **13**, 2596.
23 P. Li, B. Liu, Y. Ni, K. K. Liew, J. Sze, S. Chen and S. Shen, *Adv. Mater.*, 2015, **27**, 4585–4591.
24 P. N. Bartlett, J. J. Baumberg, S. Coyle and M. E. Abdelsalam, *Faraday Discuss.*, 2004, **125**, 117.
25 S. Zein El Abedin, A. Prowald and F. Endres, *Electrochem. Commun.*, 2012, **18**, 70–73.
26 A. L. Pokrovsky, V. Kamaev, C. Y. Li, Z. V. Vardeny, A. L. Efros, D. A. Kurdyukov and V. G. Golubev, *Phys. Rev. B*, 2005, **71**, 165114.
27 T. A. Kelf, Y. Sugawara, R. M. Cole, J. J. Baumberg, M. E. Abdelsalam, S. Cintra, S. Mahajan, A. E. Russell and P. N. Bartlett, *Phys. Rev. B*, 2006, **74**, 245415.
28 K. Jung, J. Hahn, S. In, Y. Bae, H. Lee, P. V. Pikhitsa, K. Ahn, K. Ha, J. K. Lee, N. Park and M. Choi, *Adv. Mater.*, 2014, **26**, 5924–5929.
29 P. Yang, J. Zheng, Y. Xu, Q. Zhang and L. Jiang, *Adv. Mater.*, 2016, **28**, 10508–10517.
30 M. J. Kale, T. Avanesian and P. Christopher, *ACS Catal.*, 2014, **4**, 116–128.
31 M. V. Rybin, A. B. Khanikaev, M. Inoue, K. B. Samusev, M. J. Steel, G. Yushin and M. F. Limonov, *Phys. Rev. Lett.*, 2009, **103**, 023901.
32 E. C. Le Ru and P. G. Etchegoin, *Annu. Rev. Phys. Chem.*, 2012, **63**, 65–87.
33 J. F. Li, Y. F. Huang, Y. Ding, Z. L. Yang, S. B. Li, X. S. Zhou, F. R. Fan, W. Zhang, Z. Y. Zhou, D. Y. Wu, B. Ren, Z. L. Wang and Z. Q. Tian, *Nature*, 2010, **464**, 392–395.
34 A. Ahmed and R. Gordon, *Nano Lett.*, 2012, **12**, 2625–2630.
35 D. K. Lim, K. S. Jeon, J. H. Hwang, H. Kim, S. Kwon, Y. D. Suh and J. M. Nam, *Nat. Nanotechnol.*, 2011, **6**, 452–460.
36 M. Chirumamilla, A. Toma, A. Gopalakrishnan, G. Das, R. P. Zaccaria, R. Krahne, E. Rondanina, M. Leoncini, C. Liberale, F. De Angelis and E. Di Fabrizio, *Adv. Mater.*, 2014, **26**, 2353–2358.
37 S. Coyle, M. C. Netti, J. J. Baumberg, M. A. Ghanem, P. R. Birkin, P. N. Bartlett and D. M. Whittaker, *Phys. Rev. Lett.*, 2001, **87**, 176801.
38 N. Sapoletova, T. Makarevich, K. Napolskii, E. Mishina, A. Eliseev, A. van Etteger, T. Rasing and G. Tsirlina, *Phys. Chem. Chem. Phys.*, 2010, **12**, 15414–15422.
39 R. Jin, Y. Cao, C. A. Mirkin, K. L. Kelly, G. C. Schatz and J. G. Zheng, *Science*, 2001, **294**, 1901.
40 S. Kumbhar, M. K. Kinnan and G. Chumanov, *J. Am. Chem. Soc.*, 2005, **127**, 12444–12445.
41 T. A. Kelf, Y. Sugawara, J. J. Baumberg, M. Abdelsalam and P. N. Bartlett, *Phys. Rev. Lett.*, 2005, **95**, 116802.
42 J. Dintinger, S. Klein, F. Bustos, W. L. Barnes and T. W. Ebbesen, *Phys. Rev. B: Condens. Matter Mater. Phys.*, 2005, **71**, 035424.

43 M. Tabatabaei, M. Najiminaini, K. Davieau, B. Kaminska, M. R. Singh, J. J. L. Carson and F. Lagugné-Labarthet, *ACS Photonics*, 2015, **2**, 752–759.

44 H. Liu, L. Zhang, X. Lang, Y. Yamaguchi, H. Iwasaki, Y. Inouye, Q. Xue and M. Chen, *Sci. Rep.*, 2011, **1**, 112.

45 K. Fuku, R. Hayashi, S. Takakura, T. Kamegawa, K. Mori and H. Yamashita, *Angew. Chem., Int. Ed.*, 2013, **52**, 7446–7450.

46 X. Meng, L. Liu, S. Ouyang, H. Xu, D. Wang, N. Zhao and J. Ye, *Adv. Mater.*, 2016, **28**, 6781–6803.

47 Z. Chen, X. Li, J. Wang, L. Tao, M. Long, S. J. Liang, L. K. Ang, C. Shu, H. K. Tsang and J. B. Xu, *ACS Nano*, 2017, **11**, 430–437.

48 Y. Liu, X. Zhang, J. Su, H. Li, Q. Zhang and Y. Gao, *Opt. Express*, 2014, **22**, 30148–30155.

49 P. Christopher, H. Xin, A. Marimuthu and S. Linic, *Nat. Mater.*, 2012, **11**, 1044–1050.